

First-principles study of lithium aluminosilicate glass scintillators

Ghardi, EM; Scrimshire, Alex; Smith, Robin; Bingham, PA; Middleburgh, SC; Lee, WE; Rushton, MJD

Physical Chemistry Chemical Physics

DOI:

[10.1039/D3CP05576K](https://doi.org/10.1039/D3CP05576K)

E-pub ahead of print: 30/01/2024

Peer reviewed version

[Cyswllt i'r cyhoeddiad / Link to publication](#)

Dyfyniad o'r fersiwn a gyhoeddwyd / Citation for published version (APA):

Ghardi, EM., Scrimshire, A., Smith, R., Bingham, PA., Middleburgh, SC., Lee, WE., & Rushton, MJD. (2024). First-principles study of lithium aluminosilicate glass scintillators. *Physical Chemistry Chemical Physics*, 26(7), 6138-6147. Advance online publication. <https://doi.org/10.1039/D3CP05576K>

Hawliau Cyffredinol / General rights

Copyright and moral rights for the publications made accessible in the public portal are retained by the authors and/or other copyright owners and it is a condition of accessing publications that users recognise and abide by the legal requirements associated with these rights.

- Users may download and print one copy of any publication from the public portal for the purpose of private study or research.
- You may not further distribute the material or use it for any profit-making activity or commercial gain
- You may freely distribute the URL identifying the publication in the public portal ?

Take down policy

If you believe that this document breaches copyright please contact us providing details, and we will remove access to the work immediately and investigate your claim.

First-Principles Study of Lithium Aluminosilicate Glass Scintillators

E. M. Ghardi ^a, A. Scrimshire ^b, R. Smith ^b, P. A. Bingham ^b, S. C. Middleburgh ^a, W. E. Lee ^a, and M. J. D. Rushton ^a

^a *Nuclear Futures Institute, Bangor University, Gwynedd, LL57 2DG, United Kingdom*

^b *Materials and Engineering Research Institute, College of Business, Technology and Engineering, Sheffield Hallam University, Sheffield, S1 1WB, United Kingdom*

Abstract:

Radiation sensors are an important enabling technology in several fields, such as medicine, scientific research, energy, defence, meteorology, and homeland security. Glass-based scintillators have been in use for more than 50 years and offer many benefits, including their ability to respond to different types of radiation, and to be readily formed into various shapes. There is, however, the prospect to develop new and improved glass scintillators, with low self-absorption, low refractive indices, and high radiative recombination rates. To investigate the factors limiting the improvement of glass scintillator properties, this work provides insight from atomic scale simulations of the cerium-doped lithium aluminosilicate ($\text{SiO}_2\text{-Al}_2\text{O}_3\text{-MgO-Li}_2\text{O-Ce}_2\text{O}_3$) glass scintillator system. Three glass compositions were studied using molecular dynamics and density functional theory to investigate the effect of the ratio $R_{\text{Al/M}} = \frac{[\text{Al}_2\text{O}_3]}{[\text{MgO}]+[\text{Li}_2\text{O}]}$ (with $R_{\text{Al/M}} = [0.1, 0.8 \text{ and } 1.2]$) on the structural, electronic and optical properties. For a ratio $R_{\text{Al/M}} > 1$, it has been shown that glasses with increased polymerization allow for more effective incorporation of Ce^{3+} cations. The structural analysis also showed that the bond order of Al-O can be affected in the presence of a lithium-rich environment. Electronic density of states and Bader charge analysis indicate a decline in the population of localized trapping states with increasing $R_{\text{Al/M}}$. This suggests a higher probability of radiative recombination which can increase the photon yield of these scintillators. These findings provide valuable guidance for optimizing Li-glasses in neutron detection systems by highlighting the intricate challenges.

I. Introduction

Silicate glasses have been known for decades as suitable hosts for rare-earth elements and have been extensively used for the fabrication of solid-state lasers, optical amplifiers and solar control devices ¹⁻³. The increasing demand for efficient low-cost materials, associated with ease of forming and high-volume commercial production potential, has extended their range of applications ⁴. In nuclear instrumentation, one of the central uses of rare-earth doped silicate glasses is within scintillators ⁵. These offer desirable functionalities as optical materials, such as low refractive index and high visible-light optical transmittance ⁴. In addition, silicate glasses are known to have high thermal stabilities and good rare-earth element solubility, which makes them strong candidates to replace single crystal scintillators ⁶. Glass scintillators are commercially available today ⁷ and are used for neutron radiography, neutron spectroscopy, and for α, β , X-rays and γ detection in extreme environments ^{8,9}.

One of the most widely-used series of glass scintillators used today is cerium-doped lithium aluminosilicate glasses, which were first developed by Anderson et al. and are now owned as a trademark by the UK-based manufacturer, Scintacor Ltd. ¹⁰. These glasses are known by tradenames including GS2 and GS20 and have proven to be efficient scintillators with an optimal photon yield when used for neutron detection applications ⁵. Nevertheless, as with most glass scintillators, long decay times with afterglow and low photon yield compared to single crystal scintillators narrows the range of applications in which these glasses can be used ¹¹. These limitations, closely related to the presence of disorder that attenuates the transport mechanisms of charge carriers in glasses to luminescence centres, have been extensively studied with the intention of improving the scintillation properties of rare-earth doped silicate glasses. Many solutions have been proposed, such as the use of sensitisers ¹², application of thermal treatment ¹³, pre-irradiation ¹⁴ and compositional modifications ¹⁵.

One of the main benefits of using glasses as scintillators is the strong relationship between the structure of glasses and their physical properties. In particular, aluminosilicate glasses are a glass system in which this relationship is most sensitive, which has made them important materials in many fields ¹⁶. Introducing Al_2O_3 into silica-based glass networks enhances connectivity and significantly impacts upon chemical and physical properties, leading to a mixture of tetrahedral SiO_4 units and polyhedral AlO_n structures ¹⁷. Depending on the network modifier type and content, the network is disrupted, and non-bridging oxygen (NBO) and charge compensation sites are formed due to the presence of ionic cations which stabilize the tetrahedral coordination of aluminium¹⁶. The presence or absence of charge compensation sites

directly influences the behaviour of AlO_x units, affecting their coordination polyhedra (e.g. the formation of 5- or 6-coordinated Al^{3+}) and, in some cases, leading to the formation of tri-clustered oxygen species (TO) ¹⁸. Furthermore, the ratio of aluminium to modifier (Al/Modifier, Al/M) plays a pivotal role, showcasing non-monotonic compositional dependence in various physical properties as compositions transition from peralkaline to peraluminous regions ^{19,20}.

To explore this complex relationship, this study explores the GS2 glass composition and compares it with two novel compositions, GSR1 and GSR2, designed to highlight stoichiometric changes from the peralkaline to the peraluminous regions from the GS2 composition. Our investigation sheds light on how these ratios can influence the physical properties of aluminosilicate glass scintillators, providing valuable insights into their behaviour. Atomistic simulations have emerged as invaluable tools, offering appropriate representations of glass chemistry and structure ^{21–23}. In this study, a combination of molecular dynamics (MD) simulations and density functional theory (DFT) analyses have been utilised to offer a new perspective on the structural, electronic, and optical properties of Li-aluminosilicate glasses. To the best of our knowledge, this is the first such atomistic simulation of these combined properties in multi-oxide glass scintillators.

II. Methodology & Simulation Details

The simulations presented in this work make use of classical MD simulations and DFT calculations. The MD simulations were used to analyse large bulk glasses to avoid any size effect bias that may appear in the bulk properties ²⁴. Additionally, MD was used to produce simulation cells suitable to be used as inputs for DFT calculation of the electronic structure.

II.1. MD Simulations

The rigid ionic model with partial charges was used to describe the partial covalency of the silicate system by considering atoms as point charges with short range forces acting on them. The Teter potential set was used to describe the interaction between different elements in the system²⁴. Having compatible potential parameters for oxide glass components and some rare-earth elements make Teter's potential set one of the most widely used and tested multicomponent oxide glass empirical potential sets ²⁴. The adopted potential has a form of short-range Buckingham and long-range Coulombic interaction expressed as follows:

$$V_{ij}(r) = \frac{Z_i Z_j e^2}{4\pi\epsilon_0 r_{ij}} + A_{ij} \exp(-B_{ij} r_{ij}) - \frac{C}{r^6},$$

where Z_i and Z_j represents the reduced charges of atoms i and j respectively. The A_{ij} , B_{ij} and C_{ij} are empirical parameters taken from²⁴. Since Ce^{3+} is the main scintillation activator in these glass systems and not Ce^{4+} ²⁵, only Ce^{3+} -O interactions were considered in the models produced. For the Mg-O interaction, the parameters were taken from reference²⁶.

Two sets of atomic glass structures were produced in this work. The first set was prepared with approximately 10,000 atoms while the second set was prepared with 200 atoms. The glass elements were placed with random initial positions in a cubic box where periodic boundary conditions were used in the three spatial directions. By using a time step of 1 fs, equations of motion were integrated using Verlet-velocity algorithm²⁷. The short-range interaction cutoff was set to 8.0 Å while the long-range Coulombic interaction was set to 10 Å²⁴. To avoid self-interacting atoms in the small models, both cutoffs were set to 6 Å. The calculation of the Coulombic interaction was performed using an Ewald summation with an accuracy of 10^{-5} . The melting process was started at a temperature of 5000 K in the NVT ensemble for 500 ps followed by another equilibration in the NPT ensemble for 500 ps to make sure that the systems had no memory of their initial configuration²⁸. The next step was to cool down the system temperature in the NPT ensemble from 5000 K to 300 K with a commonly used quenching rate of 1 K/ps²⁹. In the final stage, the obtained glass structures were equilibrated in the NPT ensemble for 100 ps to remove any internal stress that might remain from the fast cooling²⁹. Data collection have been performed every 1 ps in the NVT ensemble during the last run of 100 ps. All MD simulations and data analysis were performed using LAMMPS³⁰ package and OVITO³¹ respectively. Table 1 shows the glass compositions with the final densities of the glass models produced by MD.

Table 1: Composition of the Li-Aluminosilicate glasses studied in this work. The compositional details for GS2 were taken from³².

	GS2	GSR1	GSR2
SiO ₂ (% mol)	49.98	41.22	52.17
MgO (% mol)	32.50	6.45	7.04
Al ₂ O ₃ (% mol)	5.89	26.70	26.53
Ce ₂ O ₃ (% mol)	0.67	0.50	0.64
Li ₂ O (% mol)	10.96	25.13	13.61
R _{Al/M}	0.13	0.84	1.28

ρ (g/cm ³)	2.64 ± 0.01	2.61 ± 0.01	2.58 ± 0.01
-----------------------------	-----------------	-----------------	-----------------

II.2. DFT Calculations

From the MD simulations, 20 glass configurations for each composition were used as an input for DFT calculations as implemented in Vienna *ab-initio* Simulation Package (VASP) ^{33,34}. The electronic structure was described by the generalized gradient approximation using the PBE exchange-correlation functional ³⁵. The calculation was considered to have converged when the total energy changed less than 10^{-4} eV between two consecutive self-consistent iterations, and all components of ionic force were less than 0.01 eV/Å. The k-sampling in all calculations was restricted to the Γ -point and the plane waves have been included up to 600 eV. The volume of each glass configuration was optimized initially with a convergence threshold of 0.5 kbar for the components of the stress tensor. The obtained glass structures were used to calculate the electronic properties reported in this work. Table S1 shows the final densities of the optimized glass structures found by DFT.

The description of highly localized *f*-electrons in rare-earth elements is not correctly captured in DFT due to self-interaction errors ³⁶. To remedy this, calculations were performed with a Hubbard correction on Ce atoms where the 4*f* electrons are localized. The determination of the U correction value is obtained empirically for crystals ^{35,37} by adjusting its value until the energy band gap (E_{gap}) matches experimental results. For the glasses of interest, no empirical values of E_{gap} were reported. The starting point to find the correct value of U was to refer to previous studies on the systematic effect of the U term on CeO₂ and Ce₂O₃. According to Loschen et al. ³⁷, a well-balanced choice of U for GGA+U can be found to be around 2 to 3 eV with increasing the on-site Coulombic interactions by 1.5-2.5 eV.

To find a reasonable value of the U term, tests were conducted for this parameter by starting with values suggested from the literature at 2.5 eV ³⁷, and finished at a value up to 5.0 eV. Since the glasses considered in this work have different compositions, we searched mainly for a value of U where the E_{gap} can show a clear trend as a function of composition. Figure 1a shows the trend as a function of U values tested for our calculation. A variation in the trend of the relative bandgap energy is observed from glass GS2 to glass GSR1 in the range of values of U reported by the literature ³⁷, leading to a misleading trend in the compositional effect on the bandgap energies when the value of $U < 3.5$ eV. Starting from $U = 3.5$ eV, the E_{gap}

difference between the individual glasses remained the same. This is more evident in Figure 1b, which shows a clear compositional dependence on the conduction band minimum (CBM) energy level. In the conduction band, the difference between the E_{CBM} of GSR1 glass and the GS2 glass reaches a value at which the difference between the three systems become nearly constant at a value of $U = 3.5$ eV. The analysis was used to estimate a reasonable value of 3.5 eV that was subsequently used in this study.

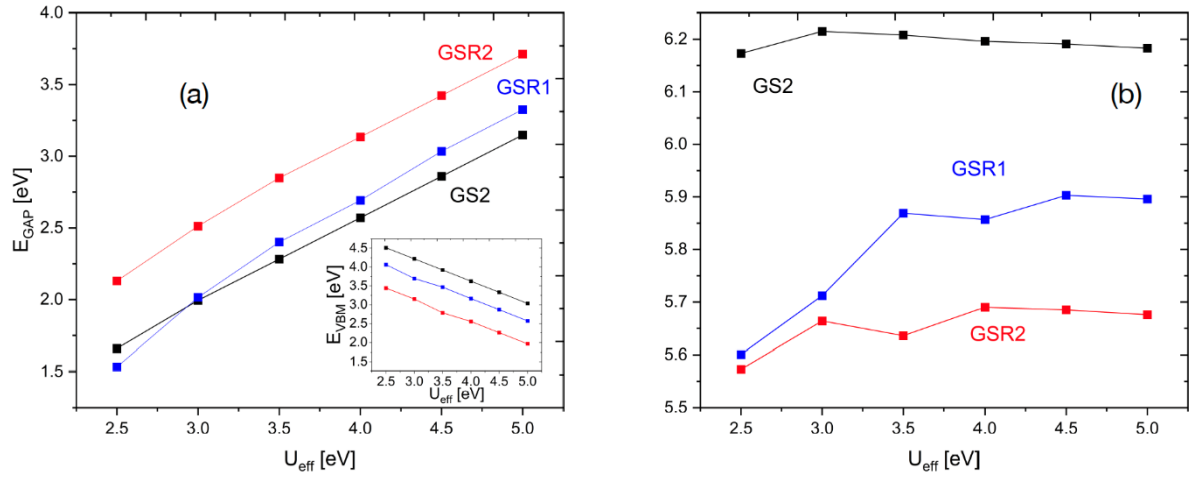


Figure 1: (a) Energy band gap calculated for different glass compositions as a function of U term. The inset shows the values of Fermi-Level energies. (b) The energies of the lowest unoccupied energy state in the conduction band for the 3 glasses.

III. Results

III.1. Structural Analysis

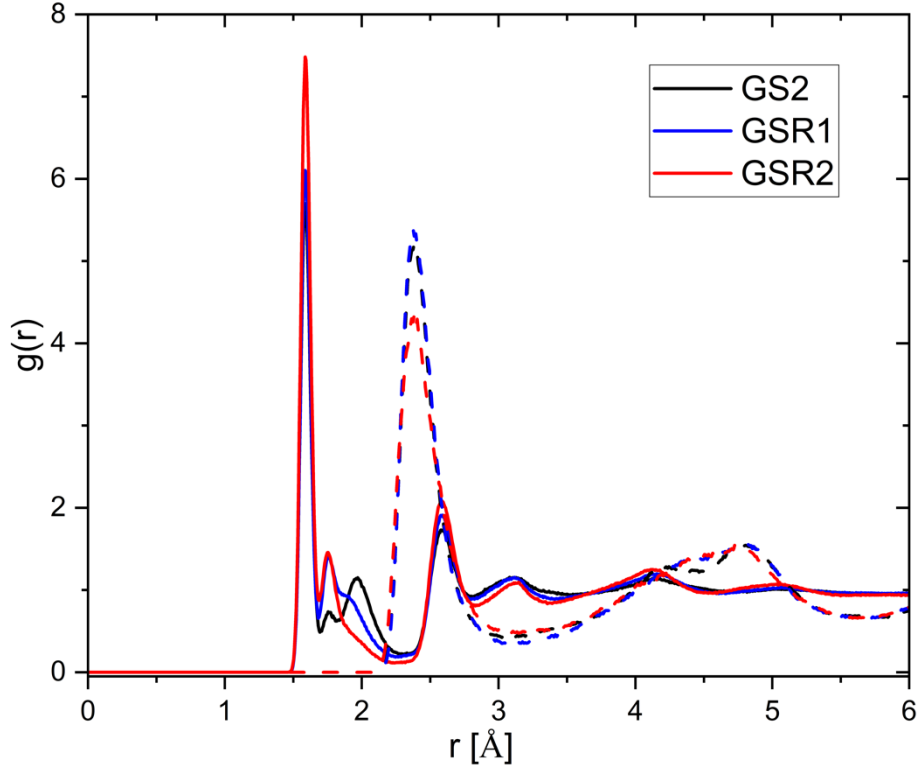


Figure 2: Radial distribution function (RDF) of the different glass compositions. The dashed lines represent the partial RDF of $\text{Ce}^{3+}\text{-O}$.

To start the structural analysis, Figure 2 shows the total and $\text{Ce}^{3+}\text{-O}$ partial radial distribution functions (RDFs) for the different glass compositions studied in this work. For the total RDF, the main peak represents the main bonding building the glass network at around 1.6 Å that corresponds to the Si-O bond length³⁸. The fluctuation of the secondary peaks between 1.7 Å and 2.0 Å shows the clear difference in composition in terms of Al-O, Li-O and Mg-O bonds³⁸, while the high peak above 2.0 Å represents a combination of $\text{Ce}^{3+}\text{-O}$ and O-O bonds³⁹. The partial RDF of $\text{Ce}^{3+}\text{-O}$ shows a main peak at 2.38 Å, in close agreement with previous simulations and experimental results³⁹⁻⁴¹.

To characterize the effect of $R_{\text{Al/M}}$ ratio on the bulk chemistry of the glass scintillator, the clustering behaviour of Ce^{3+} in the glasses was analysed. Clustering and phase separation are the main limiting constraints of rare-earth element concentration in silicate glasses⁴². It is thus important to ensure that Ce^{3+} is fully incorporated within the glass network before

characterizing other properties of the glass. Figure 3 shows the percentage of cluster size for the three glasses. We defined a cluster size in this analysis as the number of Ce^{3+} in a connected path of Ce^{3+} -O bonds. Figure 3 clearly demonstrates that Ce^{3+} is well dispersed throughout all three glasses. GSR2 exhibits the least clustering, with a value of 18.15%, followed by GSR1 with a clustering of 21.51% and GS2 with the most clustering at around 25.25 %. Large 5- and 6-membered clusters are predominantly present in glasses GSR1 and GSR2, while glass GS2 exhibits none of these clusters. The increased concentration of glass modifiers Li and Mg in glass GS2 creates more interstitial sites within the network, thus preventing the formation of large Ce^{3+} clusters. The solubility of Ce^{3+} for the GSR2 glass can be related to the glass network structure by considering that GSR1 and GS2 glasses have less polymerised structures compared to GSR2 glass.

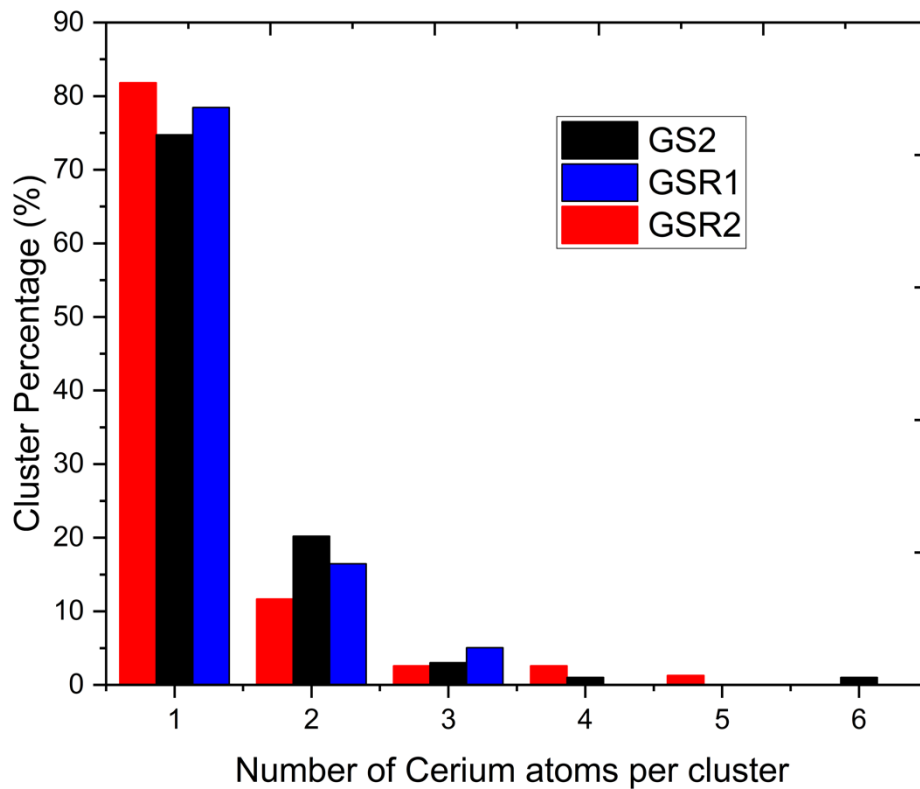


Figure 3: Cluster size distribution for GS2, GSR1 and GSR2 glasses obtained from MD simulations. The percentages were averaged over 20 different configurations.

Next, the local environment of Ce^{3+} was analysed in terms of coordination and bond angles. Figure 4a shows the percentages of Ce^{3+} coordination environment with oxygen within the three glasses. In general, the distribution of Ce^{3+} coordination environment appears symmetrical, with most cerium atoms surrounded by 7 oxygens in all three glasses. GSR2 glass

is reported to have a wider distribution of coordination states of Ce^{3+} ranging from 4 to 9 compared to GS2 and GSR1 glasses that have a 5 to 9 distribution. Another feature of GSR2 glass is that there are more undercoordinated states (4 and 5) present in the glass network, whereas the over-coordinated states (8 and 9) appear to be more populated in glasses GS2 and GSR1. According to Tian et al.⁴⁰ who studied cerium-doped silica glasses, Ce^{3+} coordination distribution ranges from 3 to 8 in the simplest case of pure vitreous silica, with an average coordination number of 5.0. By comparing these values to the work of Du et al.⁴¹ on phospho-aluminosilicate glasses, Ce^{3+} has a wider range and a higher coordination number from 5 to 8. The shifting to a higher coordination state of Ce^{3+} from pure silica can be understood from the common point between the two former mentioned systems and the GS glasses, which is the presence of aluminium.

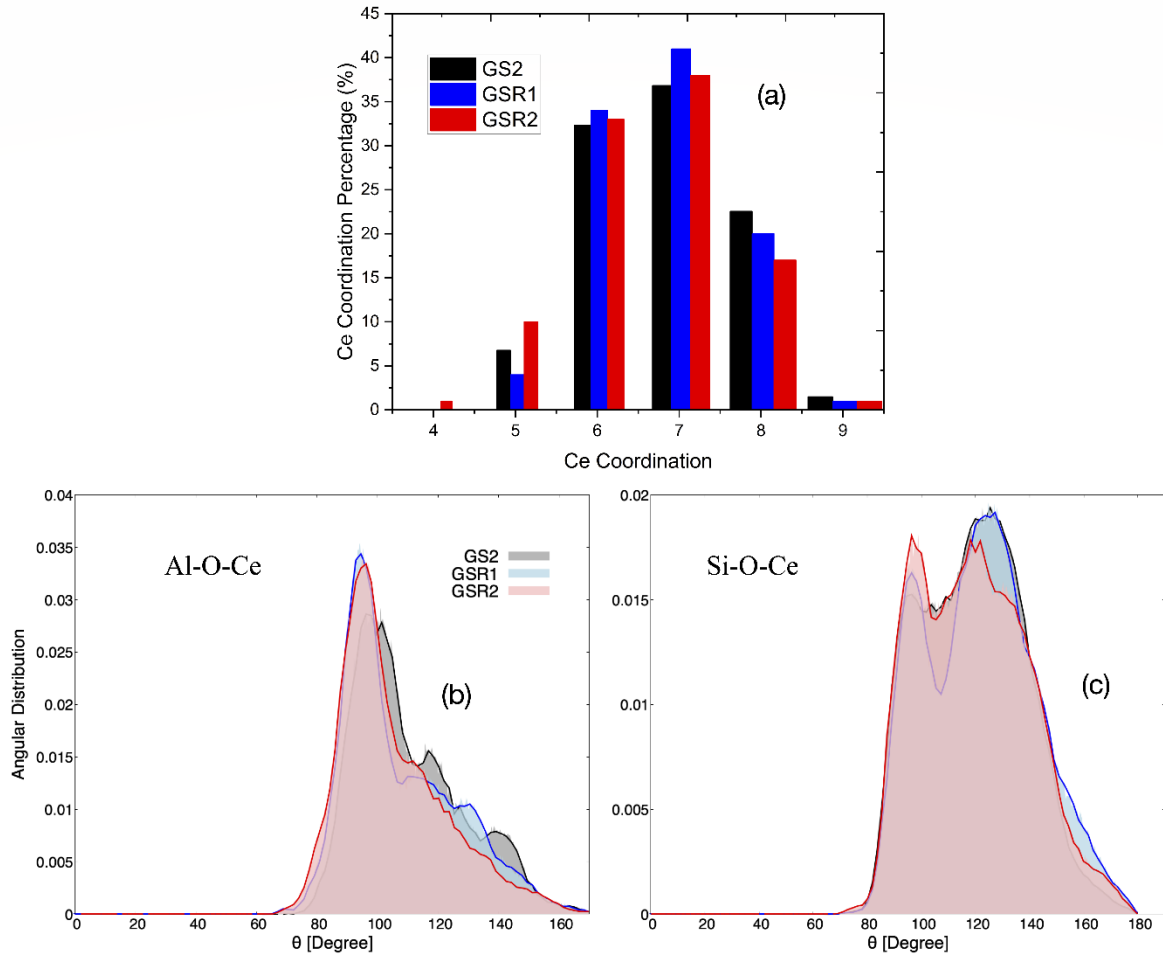


Figure 4: (a) Ce^{3+} coordination in the three glasses, (b) and (c) Angular bond distribution of Al-O- Ce^{3+} and Si-O- Ce^{3+} , respectively.

The effect of Al on Ce^{3+} is illustrated in Figure 4b, which shows the bond angle distribution of the linkage Al-O-Ce^{3+} . The bond angle distribution for the GS2 glass displays three main peaks located at around 140° , 117° and 97° . This is also true for GSR1 glass with three peaks appearing at 128° , 118° and 89° while GSR2 glass shows only one sharp peak at 91° and a shoulder at $\sim 110^\circ$ with broad tail extending to the maximum. The absence of the distinctive peaks for the GSR2 glass can be related to the charge compensating role of Ce^{3+} oxygen environment around aluminium. This charge stabilization appears in the GSR2 glass to narrow the Al-O-Ce^{3+} angle. Inspection of individual Al-O-Ce^{3+} angles showed that the main peak around 95° corresponds to an Al polyhedron sharing more than one oxygen with Ce^{3+} whilst the two other peaks above 110° correspond to the one oxygen per Al polyhedron as displayed in Figure 5.

Regarding Si surrounding Ce^{3+} , the bond angle distribution as shown in Figure 4c reveals the presence of two main peaks at round 97° and 124° for the Si-O-Ce^{3+} linkage. A similarly-shaped distribution was reported previously by Tian et al.⁴⁰ with a less pronounced tail. The two peaks were considered to be Si-BO-Ce^{3+} (BO denoting Bridging Oxygen) for angles between 75° and 150° while the remaining tail was attributed to Si-NBO-Ce^{3+} (NBO denoting Non Bridging Oxygen).

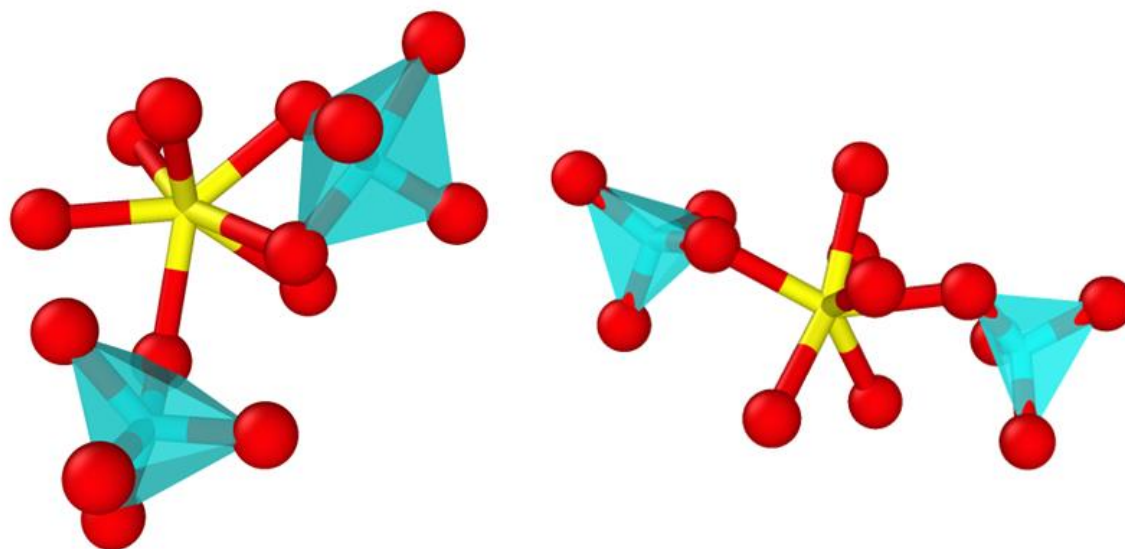


Figure 5: Illustrations of different configurations of the Al-O-Ce^{3+} bond. The red spheres represent O, the yellow centres Ce^{3+} and the Al is located in the centre of the polyhedra surrounding Ce^{3+} .

To study the connectivity and medium range structure of the glasses, the network of the glasses was explored in term of Q_n species. The n stands for the number of BO surrounding the glass formers Si and Al. Figure 6 presents the percentages of each Q_n type found within the three studied glasses. In each of the glasses studied, the shape of distribution of percentages changes,

mainly due to the ratio $R_{Al/M}$. In the case of GS2 glass with $R_{Al/M} \ll 1$, the distribution is broad and symmetric around the percentage of Q_3 . The depolymerizing effects of Li and Mg are reflected in the high percentage of Q_2 units, which tends to indicate regions of the glass network where large rings can be identified⁴³. The presence of 28% Q_4 in glass GS2 represents the pure network forming region while the presence of Q_5 in this glass can be regarded as an artifact and discounted. For the GSR1 glass, where the corresponding $R_{Al/M} \approx 1$ satisfies charge compensation rules for Al, the distribution becomes asymmetric with 60% of Q_4 and 27% of Q_3 forming the glass network. GSR2 glass has over 80% Q_4 and 13% Q_3 , while Q_2 units are nearly absent from this glass.

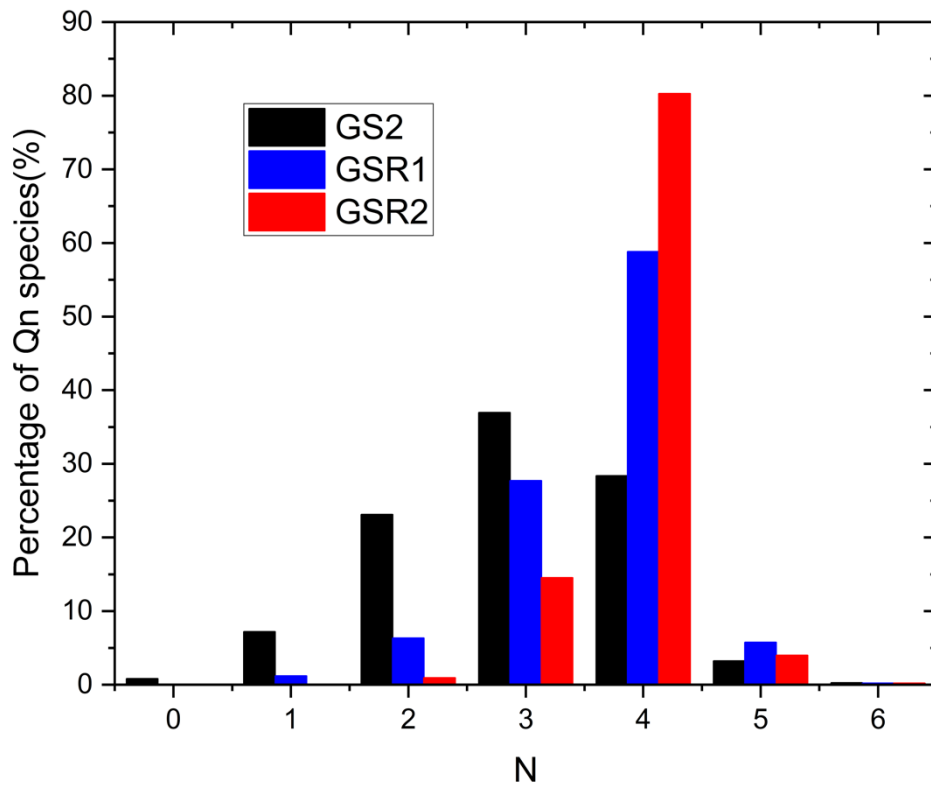


Figure 6: Q_n distribution in the three studied glasses.

III.2. Electronic Properties

As discussed in the previous section, the ratio $R_{Al/M}$ can have a major effect on the structure of the glass network. This in turn can greatly alter the electronic properties of the glass. In this section, these properties based on the small size models produced by MD simulation are investigated. As previously mentioned in Section II, the models produced in this work were constrained to include cerium as only Ce^{3+} during the MD simulations. The DFT calculations, on the other hand, were run using pseudo potentials for Ce without imposing its oxidation state. For all the configurations used for the three glasses the magnetic moment of Ce was found to

be equal to 1 on average, which successfully validates our procedure to create unpaired electrons and obtain Ce^{3+} .

The band gap details and the final densities obtained from the electronic structure calculations of the 60 glass models (20 distinct structures per composition) are represented in Table S1. For GS2 glass models, the electronic band gap ranges between 1.46 and 2.86 eV, with an average value of 2.28 eV. The valence band maximum was found to be between 2.83 and 4.01 eV and a conduction band energy between 5.24 and 6.30 eV. For GSR1 and GSR2 glasses, the electronic band gap has a value on average of 2.55 eV and 2.63 eV, respectively. No published data regarding the band gaps of these materials was found in the literature to enable direct comparison Tyrrell et al.³² provided measured GS2 glass density data, which closely matches calculated values from DFT, as indicated in Table S1.

To obtain more detail of the electronic structure of the studied glasses, the electronic densities of states (EDOS) have been analysed. This analysis allows us to determine the defects related to the electronic states arising from the lack of long-range order in glasses and amorphous materials⁴⁴. Figure 7a shows the EDOS of GS2 glass model with the closest value to the average band gap. The EDOS displays some interesting characteristics between the main valence band and the main conduction band, where small sharp peaks can be observed. Two peaks are seen near the valence band while the others are unoccupied states near the conduction band. The Ce projected DOS in Figure 7a shows that the two peaks near the valence band correspond to 4*f* orbital electrons, which represents the electronic states of the activation centres. In the conduction band, they also constitute the first band minima. The 5*d* projected DOS shows that the corresponding electronic states are mainly embedded in the conduction band and do not contribute to the potential trapping states. Regarding the second set of peaks near the conduction band, the element projected DOS reveals that all elements present in the glass bulk chemistry contribute to the appearance of this peak, which is considered to be potential electron traps. Figure 7b shows the partial charge density for electron trap state in the gap near the conduction band. It can be seen from this visual representation that the trap state is localised in a few atomic states. The local environment within which this trap states resides appears to be rich in Mg and Al, which might relate the presence of this trap state with the charge compensation role of Mg⁴⁵.

For the GSR1 glass, Figure 7b shows the EDOS with an additional type of defects but this time near the valence band. Compared to the GS2 glass, the main valence band is shifted towards lower energies, thus increasing the band gap. The electronic states of the corresponding defects in this band are located at energies lower than the occupied 4*f*Ce states observed at the Fermi

level in the projected DOS. This type of trap defect also mainly originates from the disordered nature of the glass and is primarily related to oxygen-deficient sites. Figures 7d and 7e provide a snapshot of the two types of defect present in GSR1 glasses. In Figure 7d, the electronic trapping state appears to be located around Ce^{3+} in a glass modifier-rich region. Figure 7e shows the second type of defect which is a hole trap that is created mainly on NBO sites. These sites, which contribute in the depolymerization of the glass network are also traps for the charge carriers¹³. In the case of GSR2 glass, Figure 7f shows an EDOS without any type of defect in its high polymerized structure. The main change in the overall form of the bands is observed, in this case, in the conduction band where a broadening of the lower unoccupied states is seen. In fact, in the samples generated for GS2 glass, 95% of the configurations had potential electron traps and 40% had potential hole traps. However, for GSR1 glass it was found that 80% of the configuration had electron traps while only 25% were found with hole traps. In the case of GSR2 glass, these statistics were also found to correspond to 75% for electron trapping states and 20% hole trapping states.

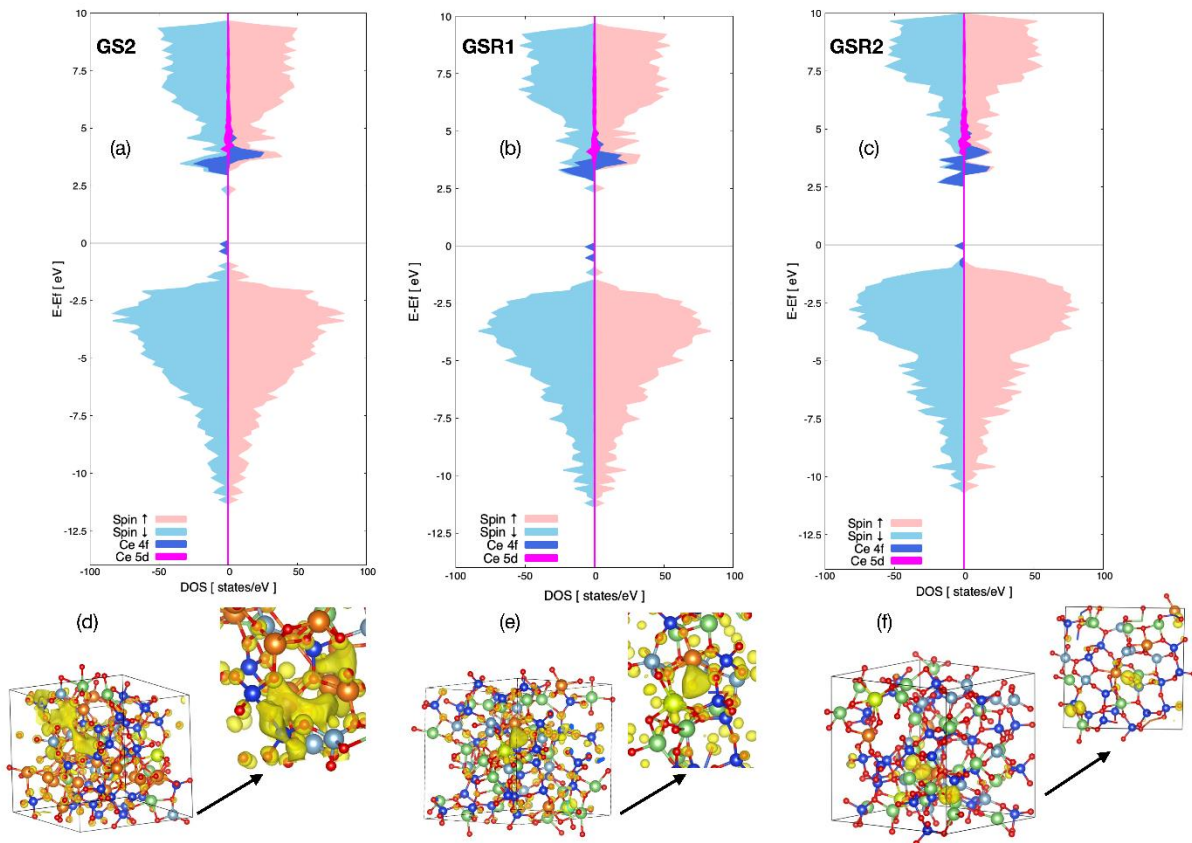


Figure 7: Electronic densities of states for glasses (a) GS2, (b) GSR1 and (c) GSR2. (d-f) Snapshots of the charge density for potential traps.

To further explore the electronic properties of the studied glasses, the nature of the bonding was investigated by calculating the bond order distribution for different bond types within the glasses. The results are reported in Figure 8. In general, for the three glasses, the bond order follows Sun's ⁴⁶ single bond strength model, with the glass former showing the strongest bond strength and the highest bond order as expected. The Al-O bonds have a lower bond order followed by Ce³⁺-O bond. The distribution of bond order of ionic Mg-O and Li-O bonds is demonstrated by the low bond order less than 0.3 and 0.2 respectively. The major observation regarding distribution of these bonds is related to the discontinuity of the Al-O bond order spread in GSR1 glass for bond lengths between 2.0 Å and 2.6 Å. This behaviour can be related to the presence of Li₂O content being similar in this glass composition to Al₂O₃. Compared to GS2 glass that has a higher content of MgO than Li₂O, the spread of Al-O bond order smoothly continues to decrease until it reaches the lowest values. Also, in the peraluminous region for the GSR2 glass, the Al-O bond order decrease smoothly to zero. This may lead to the assumption that Li is affecting more strongly the bond strength of Al-O than Mg. The insets in Figure 8 present the oxygen net charge based on Bader charge analysis ⁴⁷. The distribution shows two main peaks with different charges corresponding to BO and NBO. The BOs lose more charge from their covalent surrounding compared to NBOs, which lose less. The interplay between the composition and the charge transfer from oxygen is also illustrated in the inset of Figure 8, where a smooth change towards a lower charge is observed as a function of R_{Al/M}. A significant contrast is observed in the oxygen charge distribution, in the presence of a tail at around -1.6e. In this specific range, the distribution of oxygen charge appears to be smeared for glasses GS2 and GSR1, while a smoother tail is observed for the GSR2 glass, suggesting that the hole trapping states are localized mostly in NBOs.

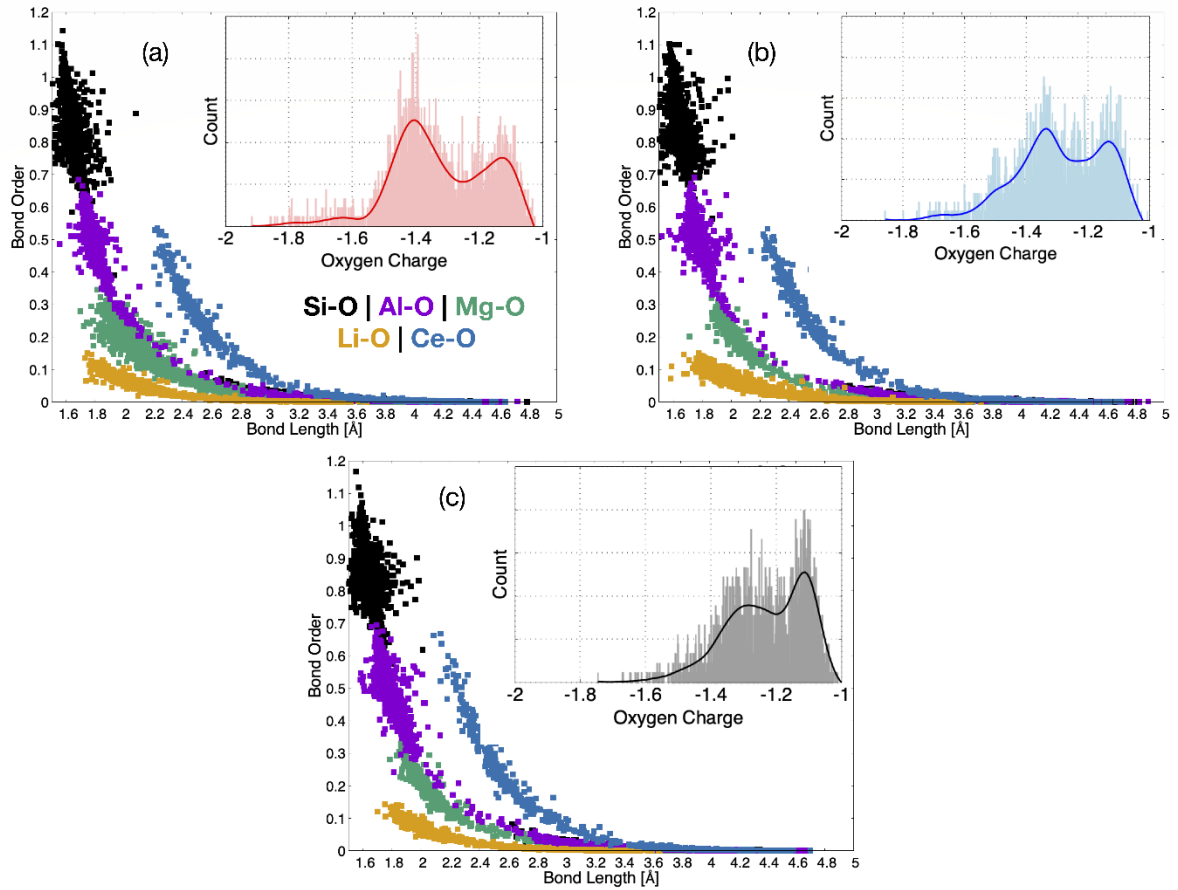


Figure 8: Bond order distribution of covalent and ionic bonds the (a) GS2, (b) GSR1 and (c) GSR2 glass.

III.3. Optical Properties

To function as an effective part of a sensor device, scintillation photons must be able to travel through the glass scintillator to its associated photomultiplier. Consequently, the optical absorption properties of the glass are important. The key quantity that can be associated with the interaction of photons with electrons is the frequency dependent dielectric function. The results for the studied glasses, in the form of the dielectric function and the energy loss function, are shown in Figure 9. The imaginary part in Figure 9a shows two main absorption peaks at around 9.87 eV and 20.33 eV for all three glasses. The main difference observed is related to the intensity of the first peak, which decreases as $R_{Al/M}$ increases. This trend is also outlined in the absorption edge, which blueshifts toward higher photon energies. The systematic dependency on composition is further illustrated in Figure 9b in the real part where the refractive index decreases. The anomalous dispersion region in the real part also shows a larger broadening for GSR2 glass compared to the other glasses.

Figure 9c shows the energy loss functions for the three glasses with more features related to the effect of $R_{Al/M}$. The plasma frequency ω_P identified from the largest peak position appears to redshift as $R_{Al/M}$ increases. For GS2 glass, ω_P was found to be 16.66 eV while for glasses GSR1 and GSR2 it was found to be 16.41 and 16.26 eV, respectively. Figure 9c also shows a clear broadening for GSR2 glass in the largest peak compared to GS2 and GSR1, also with a blueshift in the small secondary peak of the energy loss function.

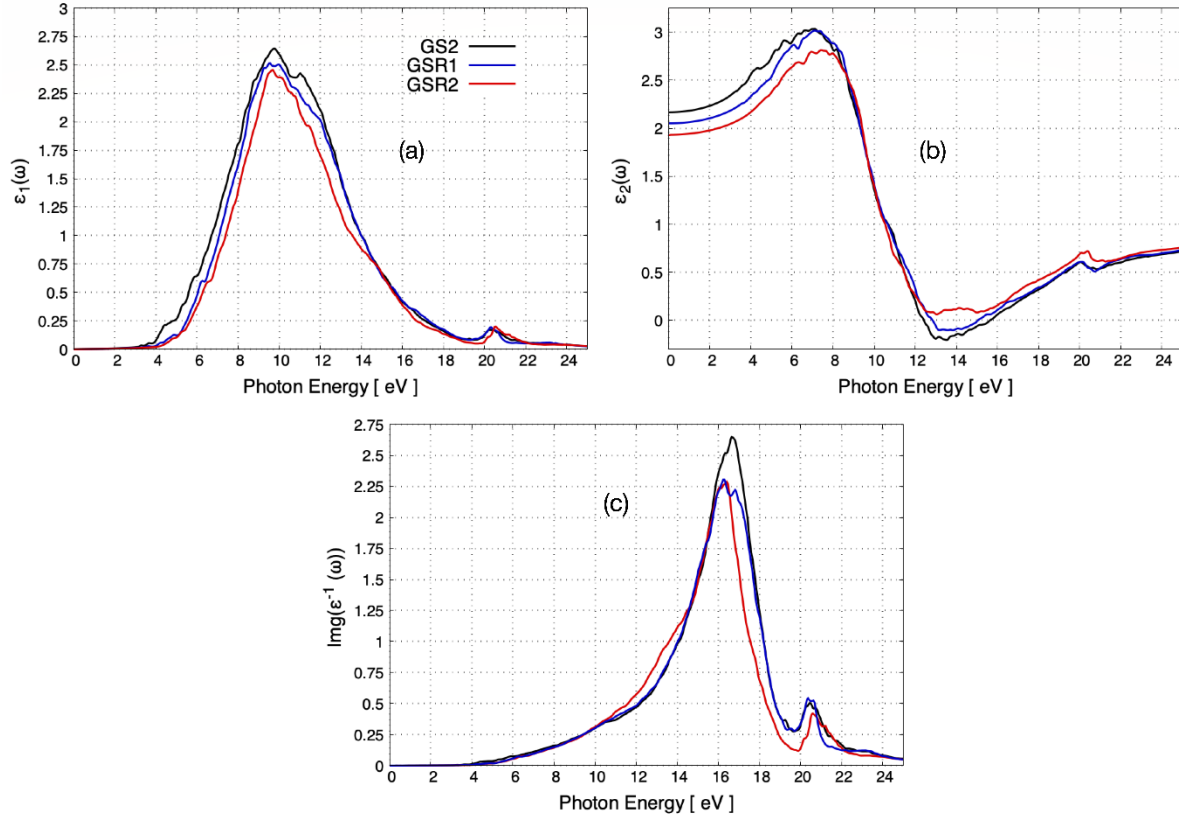


Figure 9-a) Imaginary part and (b) real part of the frequency dependent dielectric function. (c) electron-energy loss function of the three glass compositions.

IV. Conclusions

The use of glasses for neutron detection poses significant challenges, mainly caused by self-absorption and low scintillation light yield. The overlap of the emission spectrum with the absorption spectrum causes a loss of photons that reach the photon counter, thereby affecting the overall photon yield. Additionally, disorder in the glass creates trapping states, promoting non-radiative recombination over the desired radiative recombination. Achieving the necessary oxidation state for activators such as Ce, vital for creating luminescence centres, proves difficult in multi-compound glasses. To address these issues, this work explored the impact of altering the ratio of Al_2O_3 to modifiers Li_2O and MgO ($R_{Al/M}$). Increasing this ratio was found

to enhance glass network polymerization, evidenced by the rise in the Q_4 population. Investigation of Ce^{3+} solubility was also carried out and in the case of $R_{Al/M} > \sim 1$ the clustering was around 18.15 %, while for $R_{Al/M} < \sim 1$ it was over 21.51 %. Moreover, increasing $R_{Al/M}$ reduced the population of trapping states which can promote radiative recombination. This effect was more pronounced for hole trapping states, outnumbering electron trapping states in all compositions. The compositional changes also affected the Al-O bond order in GSR1 glass, highlighting the unique charge compensation role of Li compared to Mg. Bader charge analysis indicated that hole trapping states were localized in non-bridging oxygens and free oxygens in GS2 and GSR1 glasses, with a smoother charge distribution observed in the GSR2 glass. This suggested that radiative recombination could be promoted by changing the $R_{Al/M}$ from GS2 to GSR2 glass. However, alterations in the $R_{Al/M}$ had no significant impact on optical properties, except for a decrease in the refractive index in GSR2 glass, which can potentially help reduce self-absorption. These findings provide valuable insight for future research and development, guiding efforts to overcome limitations and enhance the efficiency of Li-glass-based neutron detection systems ³².

V. Acknowledgement

This work has been carried out as part of “Seeing the invisible -from neutrons to photons” project funded by ESPRC grant EP/X017362/1. The computing resources were made available via HPC Wales and Supercomputing Wales (<https://www.supercomputing.wales>).

VI. References

- 1 S. Tanabe, Rare-earth-doped glasses for fiber amplifiers in broadband telecommunication, *Comptes Rendus Chimie*, 2002, **5**, 815–824.
- 2 Y. Lin, Z. Tang, Z. Zhang, J. Zhang and Q. Chen, Preparation and properties of photoluminescent rare earth doped SrO–MgO–B₂O₃–SiO₂ glass, *Materials Science and Engineering: B*, 2001, **86**, 79–82.
- 3 E. Snitzer, Optical Maser Action of Nd ³⁺ in a Barium Crown Glass, *Phys Rev Lett*, 1961, **7**, 444–446.
- 4 R. L. Leonard and J. A. Johnson, Scintillator Glasses, *Springer Handbooks*, 2019, 1555–1584.
- 5 A. R. Spowart, Measurement of the absolute scintillation efficiency of granular and glass neutron scintillators, *Nuclear Instruments and Methods*, 1969, **75**, 35–42.

- 6 J. Liu, X. Zhao, Y. Xu, H. Wu, X. Xu, P. Lu, X. Zhang, X. Zhao, M. Xia, J. Tang and G. Niu, All-Inorganic Glass Scintillators: Scintillation Mechanism, Materials, and Applications, *Laser Photon Rev*, 2023, **17**, 2300006.
- 7 Lithium Glass Scintillators | Crystals, <https://www.crystals.saint-gobain.com/radiation-detection-scintillators/crystal-scintillators/lithium-glass-scintillators>, (accessed 24 January 2022).
- 8 Y. Zou, W. Zhang, C. Li, Y. Liu and H. Luo, Construction and test of a single sphere neutron spectrometer based on pairs of ^6Li -and ^7Li -glass scintillators, *Radiat Meas*, 2019, **127**, 106148.
- 9 Z. T. Kang, R. Rosson, B. Barta, C. Han, J. H. Nadler, M. Dorn, B. Wagner and B. Kahn, $\text{GdBr}_3\text{:Ce}$ in glass matrix as nuclear spectroscopy detector, *Radiat Meas*, 2013, **48**, 7–11.
- 10 6-Lithium Enriched Glass Scintillators | Products | Scintacor, <https://scintacor.com/products/6-lithium-glass/>, (accessed 24 January 2022).
- 11 T. Murata, Y. Arikawa, K. Watanabe, K. Yamanoi, M. Cadatal-Raduban, T. Nagai, M. Kouno, K. Sakai, T. Nakazato, T. Shimizu, N. Sarukura, M. Nakai, T. Norimatsu, H. Nishimura, H. Azechi, A. Yoshikawa, S. Fujino, H. Yoshida, N. Izumi, N. Sato and H. Kan, Fast-response and low-afterglow cerium-doped lithium 6 fluoro-oxide glass scintillator for laser fusion-originated down-scattered neutron detection, *IEEE Trans Nucl Sci*, 2012, **59**, 2256–2259.
- 12 Y. Chen, D. Luo, L. Luo, X. Wang, T. Tang and W. Luo, Luminescence of $\text{Ce}^{3+}/\text{Tb}^{3+}$ ions in lithium–magnesium aluminosilicate glasses, *J Non Cryst Solids*, 2014, **386**, 124–128.
- 13 M. Bliss, R. A. Craig and P. L. Reeder, The physics and structure-property relationships of scintillator materials: effect of thermal history and chemistry on the light output of scintillating glasses, *Nucl Instrum Methods Phys Res A*, 1994, **342**, 357–363.
- 14 I. Veronese, C. De Mattia, M. Fasoli, N. Chiodini, M. C. Cantone, F. Moretti, C. Dujardin and A. Vedda, Role of Optical Fiber Drawing in Radioluminescence Hysteresis of Yb-Doped Silica, *Journal of Physical Chemistry C*, 2015, **119**, 15572–15578.
- 15 H. Masai, H. Kimura, M. Akatsuka, T. Kato and T. Yanagida, Correlation between luminescence of cerium and chemical compositions in lithium silicate-based glasses, *Opt Mater (Amst)*, 2021, **121**, 111631.

- 16 L. Cormier, in *Encyclopedia of Materials: Technical Ceramics and Glasses*, Elsevier, 2021, pp. 496–518.
- 17 A. Atila, E. M. Ghardi, A. Hasnaoui and S. Ouaskit, Alumina effect on the structure and properties of calcium aluminosilicate in the percalcic region: A molecular dynamics investigation, *J Non Cryst Solids*, 2019, **525**, 119470.
- 18 J. F. Stebbins, J. V Oglesby and S. Kroeker, Oxygen triclusters in crystalline CaAl_4O_7 (grossite) and in calcium aluminosilicate glasses: ^{17}O NMR, *American Mineralogist*, 2001, **86**, 1307–1311.
- 19 J. O. Isard, Electrical conduction in the aluminosilicate glasses, *J. Soc. Glass Technol*, 1959, **43**, 113–231.
- 20 D. E. Day and G. U. Y. E. Rindone, Properties of Soda Aluminosilicate Glasses: I, Refractive Index, Density, Molar Refractivity, and Infrared Absorption Spectra, *Journal of the American Ceramic Society*, 1962, **45**, 489–496.
- 21 S. C. Middleburgh, W. E. Lee and M. J. D. Rushton, Structure and properties of amorphous uranium dioxide, *Acta Mater*, 2021, **202**, 366–375.
- 22 M. J. D. Rushton, I. Ipatova, L. J. Evitts, W. E. Lee and S. C. Middleburgh, Stoichiometry deviation in amorphous zirconium dioxide, *RSC Adv*, 2019, **9**, 16320–16327.
- 23 M. W. Owen, M. J. D. Rushton, M. W. D. Cooper, E. M. Ghardi, A. Claisse, W. E. Lee and S. C. Middleburgh, Modelling the impact of configurational entropy on the stability of amorphous SiO_2 , *Scr Mater*, 2023, **233**, 115507.
- 24 J. Du, Challenges in Molecular Dynamics Simulations of Multicomponent Oxide Glasses, *Springer Series in Materials Science*, 2015, **215**, 157–180.
- 25 A R Spowart, Energy transfer in cerium-activated silicate glasses, *Journal of Physics C: Solid State Physics*, 1979, **12**, 3369.
- 26 N. M. A. Krishnan, R. Ravinder, R. Kumar, Y. Le Pape, G. Sant and M. Bauchy, Density–stiffness scaling in minerals upon disordering: Irradiation vs. vitrification, *Acta Mater*, 2019, **166**, 611–617.
- 27 L. Verlet, Computer ‘Experiments’ on Classical Fluids. I. Thermodynamical Properties of Lennard-Jones Molecules, *Physical Review*, 1967, **159**, 98.
- 28 A. Atila, S. Ouaskit and A. Hasnaoui, Ionic self-diffusion and the glass transition anomaly in aluminosilicates, *Physical Chemistry Chemical Physics*, 2020, **22**, 17205–17212.

- 29 J. Habasaki, C. León and K. L. Ngai, Dynamics of Glassy, Crystalline and Liquid Ionic Conductors, *Topics in Applied Physics*, , DOI:10.1007/978-3-319-42391-3.
- 30 S. Plimpton, Fast Parallel Algorithms for Short-Range Molecular Dynamics, *J Comput Phys*, 1995, **117**, 1–19.
- 31 A. Stukowski, Visualization and analysis of atomistic simulation data with OVITO—the Open Visualization Tool, *Model Simul Mat Sci Eng*, 2009, **18**, 015012.
- 32 G. C. Tyrrell, Phosphors and scintillators in radiation imaging detectors, *Nucl Instrum Methods Phys Res A*, 2005, **546**, 180–187.
- 33 G. Kresse and J. Hafner, Ab initio molecular dynamics for liquid metals, *Phys Rev B*, 1993, **47**, 558.
- 34 G. Kresse and J. Furthmüller, Efficient iterative schemes for ab initio total-energy calculations using a plane-wave basis set, *Phys Rev B*, 1996, **54**, 11169.
- 35 J. P. Perdew, K. Burke and M. Ernzerhof, Generalized Gradient Approximation Made Simple, *Phys Rev Lett*, 1996, **77**, 3865.
- 36 S. Lutfalla, V. Shapovalov and A. T. Bell, Calibration of the DFT/GGA+U Method for Determination of Reduction Energies for Transition and Rare Earth Metal Oxides of Ti, V, Mo, and Ce, *J Chem Theory Comput*, 2011, **7**, 2218–2223.
- 37 C. Loschen, J. Carrasco, K. M. Neyman and F. Illas, First-principles LDA+U and GGA+U study of cerium oxides: Dependence on the effective U parameter, *Phys Rev B Condens Matter Mater Phys*, , DOI:10.1103/PhysRevB.75.035115.
- 38 A. Atila, E. M. Ghardi, S. Ouaskit and A. Hasnaoui, Atomistic insights into the impact of charge balancing cations on the structure and properties of aluminosilicate glasses, *Phys Rev B*, 2019, **100**, 144109.
- 39 J. L. Rygel, Y. Chen, C. G. Pantano, T. Shibata, J. Du, L. Kokou, R. Woodman and J. Belcher, Local Structure of Cerium in Aluminophosphate and Silicophosphate Glasses, *Journal of the American Ceramic Society*, 2011, **94**, 2442–2451.
- 40 Y. Tian, W. Han, X. Yuan, D. Hu, W. Zheng, Q. Zhu and F. Wang, Structure and vibrations of cerium in silica glass from molecular dynamics simulations, *Journal of the American Ceramic Society*, 2021, **104**, 208–217.
- 41 J. Du, L. Kokou, J. L. Rygel, Y. Chen, C. G. Pantano, R. Woodman and J. Belcher, Structure of Cerium Phosphate Glasses: Molecular Dynamics Simulation, *Journal of the American Ceramic Society*, 2011, **94**, 2393–2401.
- 42 L.-L. Lee and D.-S. Tsai, Ion clustering and crystallization of sol-gel-derived erbium silicate glass, *JMSL*, 1994, **13**, 615–617.

- 43 E. M. Ghardi, A. Atila, M. Badawi, A. Hasnaoui and S. Ouaskit, Computational insights into the structure of barium titanosilicate glasses, *Journal of the American Ceramic Society*, 2019, **102**, 6626–6639.
- 44 K. Konstantinou, F. C. Mocanu, T. H. Lee and S. R. Elliott, Revealing the intrinsic nature of the mid-gap defects in amorphous Ge₂Sb₂Te₅, *Nature Communications* 2019 *10:1*, 2019, **10**, 1–10.
- 45 B. Deng, Y. Shi, Q. Zhou and M. Bauchy, Revealing the structural role of MgO in aluminosilicate glasses, *Acta Mater*, 2022, **222**, 117417.
- 46 K.-H. Sun, FUNDAMENTAL CONDITION OF GLASS FORMATION, *Journal of the American Ceramic Society*, 1947, **30**, 277–281.
- 47 S. Adnan, W. Abood, W. Abdulmuhsin, W. Tang, E. Sanville and G. Henkelman, A grid-based Bader analysis algorithm without lattice bias, *Journal of Physics: Condensed Matter*, 2009, **21**, 084204.